Monthly Notices
of the
ROYAL ASTRONOMICAL SOCIETY

MNRAS **485,** 1938–1946 (2019)
Advance Access publication 2019 February 7

doi:10.1093/mnras/stz347

The study of extended emission in a radio galaxy detected in the LOFAR Two-Metre Sky Survey

S. A. Thwala,[1]★ N. Shafi,[1,2]★ S. Colafrancesco,[1]† F. Govoni[3] and M. Murgia[3]

[1]*School of Physics, University of the Witwatersrand, Johannesburg, Private Bag 3, WITS-2050, South Africa*
[2]*South African Radio Astronomy Observatory, Krugersdorp 1740, South Africa*
[3]*INAF – Osservatorio Astronomico di Cagliari Via della Scienza 5, I-09047 Selargius (CA), Italy*

Accepted 2019 January 30. Received 2019 January 16; in original form 2018 May 15

ABSTRACT

We performed a search for extended radio sources in the Low-Frequency Array Two-Meter Survey HETDEX Spring Field, and we were able to identify 11 low-brightness extended sources. In this paper we focus on the poorly studied radio galaxy PGC2285791, presenting a detailed analysis of its core, its two extended radio lobes, a spectral index map between 141 and 1400 MHz, and the multifrequency association with its IR and optical counterparts. Our results led to the identification of this source with a $z = 0.14$ extended radio galaxy exhibiting bubble-like radio lobe structures (∼6 arcmin in the S–N direction).

Key words: techniques: image processing – surveys – galaxies: general – galaxies: jets – radio continuum: galaxies.

1 INTRODUCTION

Low-frequency radio continuum observations of (radio) galaxies are very important because the associated synchrotron emission probes the aged and low-energy electrons, which are less affected by energy losses, and therefore, can propagate further away from their site of origin (assuming that the diffusion coefficient does not vary with particle energy; Mulcahy et al. 2014). Depending on the magnetic field strength and spatial extension, one would expect to see a large radio synchrotron emission in extended sources [Mulcahy et al. 2014; see also the case of the ∼700 kpc remnant radio galaxy J1828+49 (Brienza et al. 2016)] studied with the Low-Frequency Array (LOFAR; van Haarlem et al. 2013).

This is in fact the case for radio galaxies with jets or outflows: active galactic nucleus (AGN)-powered radio galaxies have relativistic jets extended and collimated for tens to hundreds of kpc. Outflows are observed to be populated by lower energy electrons which produce irregularly shaped radio lobes that typically extend for smaller distances from the galaxy core.

With the mechanism of particle (re)acceleration and physical processes that produce radio outflows still open to speculation, these sources are ideal candidates for probing the relativistic and magnetized plasma dynamics of the cosmic ray electrons with the host galaxy's interstellar medium (ISM). This interaction, between the core of the source and the ISM, can also probe the energy associated with large-scale gas outflows driven by high-energy phenomenon in an AGN (e.g. Fanti & Fanti 1994; O'Dea et al. 2002; Holt et al. 2006; Holt, Tadhunter & Morganti 2008). Therefore, radio galaxies that exhibit overlapping features between AGNs and outflow properties are crucial to filling in the gaps in our understanding of galaxy formations.

Studying the morphologies of radio lobes can give insights into the interaction between the beamed plasma emanating from an AGN and the surrounding ambient medium (Subrahmanyan, Saripalli & Hunstead 1996). Since synchrotron emission follows a power law, it is believed that the ambient medium has a higher contribution at lower frequencies. The morphology of radio sources at different frequencies can then be a tracer of the plasma's dynamical states. Using spectral index analysis we can further probe the acceleration and cooling mechanisms that operate on the cosmic ray electrons of this plasma and/with the ambient medium.

Thus, the improved sensitivity and resolution of modern low-frequency radio continuum observations can provide powerful tools to study the evolution and relation between the core of radio continuum sources, the cosmic ray electrons driving the lobes, and the ambient medium that surrounds the source. They also can provide detailed insights into the processes that regulate these different regions and their evolutionary time-scales.

In order to search and study new extended emissions around radio galaxies, we used the LOFAR Two-metre Sky Survey (LoTSS; Shimwell et al. 2017) in the still poorly explored low-frequency region of the electromagnetic spectrum. Exploring the HETDEX Spring Field (see Section 2 for details), we were able to identify 11 extended sources for our study in a region of $9.5^\circ \times 8.7^\circ$, an area of the sky comprised between α_{J2000}: $10^h37^m00^s$ to $11^h48^m00^s$ and δ_{J2000}: $+44^\circ19'00''$ to $+52^\circ55'00''$.

In this paper, we present the analysis of the diffuse emission from these sources at low frequency, and focus on the properties

★ E-mail: Siphiwe.Thwala@wits.ac.za (SAT); Nebiha.Shafi@wits.ac.za (NS)

† We honour the memory of Prof. Sergio Colafrancesco, who contributed to the paper.

and the nature of a specific radio galaxy, PGC2285791, which shows a bubble-like symmetric radio lobe structure with a prominent radio core. Our study will use the improved sensitivity of the available radio surveys (in particular the LoTSS) and their ability to better resolve radio galaxies for studies of magnetic fields, cosmic ray diffusion and particle acceleration mechanisms in their jets/lobes.

The structure of this paper is as follows: we describe in Section 2 the different data sets we use in our analyses and in Section 3 we describe the data analysis techniques. We discuss in Section 4 the identification of the extended radio sources extracted from the LoTSS and we study in particular the nature of the extended radio galaxy PGC2285791. We then discuss our results and draw our conclusion in the final Section 5.

We adopt a flat, vacuum-dominated cosmology with $H_0 = 73\,\mathrm{km\,s^{-1}\,Mpc^{-1}}$, $\Omega_{\mathrm{matter}} = 0.27$, and $\Omega_{\mathrm{vacuum}} = 0.73$.

2 DATA

We searched for extended sources in the LoTSS in order to characterize the morphology, integrated spectra, and spectral index maps of poorly known or unidentified extended radio sources. We then looked at the different available imaging surveys and used the open data across multifrequency in order to identify and characterize these sources. Specifically, in our analysis we used publicly available data from the Faint Images of the Radio Sky at Twenty-cm (FIRST; Becker et al. 1995), LoTSS, NRAO Very Large Array (VLA) Sky Survey (NVSS; Condon et al. 1998), the TIFR GMRT Sky Survey Alternative Data Release 1 (TGSS ADR1; Intema et al. 2017), VLA Low-frequency Sky Survey Redux (VLSSr; Lane et al. 2014), Wide-field Infrared Survey Explorer (WISE; Wright et al. 2010), ESO Online Digitized Sky Survey 2 (ESO-DSS2-red), and Sloan Digital Sky Survey (SDSS; Blanton et al. 2017) surveys.

The differences in resolutions and sensitivities across these surveys necessitated a careful selection criteria for deciding which surveys to use in this study. For instance, the resolution of the TGSS ADR1 is an ideal match to the LoTSS survey, however, the integration time per pointing for TGSS ADR1 is 15 min while LoTSS has 8 h, thus reducing the sensitivity of TGSS ADR1 to faint extended emission features. These differences make it challenging to correctly characterize the morphology of the extended radio sources and hinder the creation of reliable spectral index maps (since some of the structures which are present in the LoTSS are not detected to a similar extent in the TGSS ADR1). The difference in sensitivities also had to be factored in, since most of the sources have brightnesses below 0.1 Jy beam^{-1}, which is the typical noise level for the VLSSr.

With these restrictions in mind, we opted to use the LoTSS survey in conjunction with the NVSS survey to characterize the morphology of the extended sources and create spectral index maps, seeing that both surveys can resolve extended sources well. However, we noted that the resolutions of the two surveys do not match perfectly, with the NVSS survey having a lower angular resolution of 45 arcsec compared to the higher angular resolution of 25 arcsec for the LoTSS survey. To mitigate this difference we smoothed the LoTSS images to match the angular resolution of the NVSS images.

In the following we will briefly describe each one of the data sets used in our analysis.

The LoTSS is a deep imaging survey that has been obtained using a compact core and long baselines at the LOFAR observatory

Table 1. Summary of the continuum images of PGC2285791 used in this work.

Survey	Frequency (MHz)	Synthesized beam size (arcsec)	σ_{rms} (mJy beam^{-1})	Obs. date
(1)	(2)	(3)	(4)	(5)
VLSSr	73.79	75	71.15	2003 Sep. 20
LoTSS	141.5	25	0.58	2014 Jun. 13
TGSS ADR1	147.5	25	2.99	2016 Mar. 15
NVSS	1400	45	0.57	1993 Nov. 15
FIRST	1400	5	0.18	1997 Mar. 25

Table 2. List of flux densities and their respective errors of PGC2285791 for the core and source at different frequencies.

Frequency (MHz)	Flux density (mJy)	
	S_{core}	S_{source}
(1)	(2)	(3)
73.79	213.45[a] ± 32.02	213.45 ± 32.02
141.5	8.74 ± 1.11	301.20 ± 30.12
147.5	13.02 ± 3.04	28.40 ± 10.56
1400	3.40 ± 1.07	45.93 ± 4.59
1400	2.10 ± 0.25	-

Note: [a]Calculated 3σ upper limit, for the VLSSr image specified in Table 1.

observed in the frequency range of 120–168 MHz (Shimwell et al. 2017). This design allows for observations with excellent sensitivity to both extended and compact emissions, producing images that are significantly more sensitive than those produced by other existing large-area low-frequency surveys (Shimwell et al. 2017).

The products we used from the survey are the preliminary released images, which are created using a fully automated but direction-independent calibration strategy, observed at 141 MHz with a resolution of 25 arcsec and typical noise levels of less than 0.5 mJy beam^{-1} (Shimwell et al. 2017). Most of the following investigations were largely guided by observations from this survey, and all the other data were used as follow ups/complements to this imaging survey.

The survey covers an area over 350 deg^2, in the region of the HETDEX Spring Field (α_{J2000}: $10^{\mathrm{h}}45^{\mathrm{m}}00^{\mathrm{s}}$ to $15^{\mathrm{h}}30^{\mathrm{m}}00^{\mathrm{s}}$ and δ_{J2000}: $+45^{\circ}00'00''$ to $+57^{\circ}00'00''$) (Shimwell et al. 2017). Within this area, our search was focused on the P7-Mosaic (with matching coordinates of the sky area provided in Section 1). The P7-Mosaic was partitioned into smaller regions that cover 3 deg^2 to make it easier to survey the region for interesting sources. We had a particular interest in the region limited by α_{J2000}: $10^{\mathrm{h}}50^{\mathrm{m}}00^{\mathrm{s}}$ to $11^{\mathrm{h}}35^{\mathrm{m}}00^{\mathrm{s}}$ and δ_{J2000}: $+45^{\circ}00'00''$ to $+52^{\circ}00'00''$, since we initially noted the existence of the extended radio source PGC2285791 that is not characterized well previously. We searched for low surface brightness extended radio sources in this region and were able to identify the LoTSS extended radio sources listed in Table A1.

The FIRST, NVSS, and VLSSr radio surveys were conducted using the 27 reconfigurable radio antennas of the VLA. The FIRST survey was carried out at a frequency of 1400 MHz using the B configuration of the VLA, producing images with an angular resolution of 5 arcsec, typical noise levels that are less than 0.13 mJy beam^{-1} and a survey flux density threshold of about 1 mJy (Becker et al. 1995). We used the products from this survey to

locate the source positions of the optical counterparts and study the integrated spectra analysis for the radio sources selected from the LoTSS.

The NVSS survey was conducted at a frequency of 1400 MHz using the compact D and DnC configurations of the VLA to produce continuum and linear-polarization images with angular resolution of 45 arcsec, typical noise levels that are less than 0.5 mJy beam^{-1} and a point source flux density limit of about 2.5 mJy (Condon et al. 1998). We used the products from this survey to study the extent of the diffuse emission, perform integrated spectra analysis, characterize the morphology, and create spectral index maps of the extended radio sources.

The VLSSr is an imaging survey which used the VLSS catalogue as a sky model to correct for the ionospheric distortions in the data and then created a new set of sky maps and a corresponding catalogue at 73.8 MHz (Lane et al. 2014). This survey used the B and BnA configurations of the VLA to produce images with angular resolution of 75 arcsec and typical noise levels of less than 0.1 Jy beam^{-1} (Lane et al. 2014). In this work we used the products from this survey to study the integrated spectra for the radio sources selected from the LoTSS.

The TGSS ADR1 is an imaging survey of the 150 MHz radio sky, using the GMRT, aimed at producing a reliable compact source survey (Intema et al. 2017). The products used from the survey have a resolution of 25 arcsec and typical noise levels of less than 5 mJy beam^{-1} (Intema et al. 2017). These were then used to perform integrated spectra analysis, because the short integration time could not map out the diffuse emission sufficiently well.

3 DATA ANALYSIS

Radio continuum images were downloaded for each of the surveys considered here.[1,2,3,4,5]

Once the sources were identified as likely astrophysical sources, we used the Python Blob Detector and Source Finder (PyBDSF), a tool designed to decompose radio interferometry images into sources and make available their properties for further use (Mohan & Rafferty 2015). Apart from the source finding purposes, we also used this tool to calculate the rms values, perform basic error data analysis and calculate the integrated flux density for each individual data cube. The rms value obtained for each continuum image was then used as the sigma clipping levels for that corresponding image in our analysis (see discussion in Section 4 below).

To regrid our image datasets to the same grid, we used MIRIAD a data reduction and analysis software (Sault, Teuben & Wright 1995). We further used this data reduction package to smooth the LoTSS beam to the NVSS beam, to better match the angular resolution of the two surveys. Both of the above-mentioned steps were carried out in preparation for the derivation of the spectral index map (see Section 4.1.5).

3.1 Images

Most of the image calibration, cleaning, systematic checks (e.g. RFI flagging), and direction-dependent calibration (DDC) were carried out by the respective survey teams. The only exception to this treatment is that the direction-dependent calibration step still needs to be carried out for the LoTSS, and this will be part of a proposed future data release (Shimwell et al. 2017).

However, looking at the noise levels and image resolution of the different surveys considered here, we decided to use the LoTSS without performing the direction-dependent calibration because as the sigma clipping levels are increased most of the observed artefacts are clipped. This procedure however does not completely fix the errors in the shape of the sources and thus introduces an error at the edges of our spectral index maps (see our discussion of the spectral index map shown in Fig. 5).

We note that for regions closer to the core of the sources analysed, the results are more reliable because the region is detected from both surveys, i.e. the NVSS and LoTSS surveys in this instance. However, as the emission moves towards the edges of the extended emission region, the results serve as a guide since some of the telescopes are not sensitive to faint emissions and some surveys do not resolve the sources well enough.

In this respect, our study can be considered as a path-finder study for the search and characterization of extended radio sources where we kept in mind that some of the details of the peripheral extension of the radio sources we are interested in may be affected by DDC effects.

To create a more complete astrophysical characterization of the selected sources, we also looked at the counterparts of the sources in the infrared and optical wavelengths using the WISE, ESO-DSS2-red, and SDSS catalogues, respectively. This analysis was then extended to perform cross-correlations at multiwavelengths to check the consistency of our results with the information available in the literature.

Finally, in order to obtain the stellar population properties of the specific radio galaxy PGC2285791, we applied a full spectral fitting code, and derived age, metallicity, star formation rate (SFR), and black hole mass (see Section 4.1.4).

4 EXTENDED SOURCES

Our strategy for the deep search was to look for faint extended sources, since they would have not been picked up by previous studies. The sources found in our search are listed in Table A1 .

The integrated flux density uncertainties were computed using the relation:

$$\sigma_{S_\nu} = \sqrt{(\sigma_{\rm cal} S_\nu)^2 + \left(\sigma_{\rm rms}\sqrt{N_{\rm beam}}\right)^2}, \quad (1)$$

where $\sigma_{\rm cal}$ is the uncertainty in the calibration of the flux scale, S_ν is the integrated flux density at the observed frequency ν, $\sigma_{\rm rms}$ is the rms of the image, and $N_{\rm beam}$ is the number of independent beams in the source (Cantwell et al. 2016). $\sigma_{\rm cal}$ is taken to be 10 per cent for the LoTSS, NVSS, and TGSS ADR1 surveys (Condon et al. 1998; Intema et al. 2017; Shimwell et al. 2017) and 15 per cent for the VLSSr survey (Lane et al. 2014). The $\sigma_{\rm rms}$ was calculated for each source, using continuum images with a field of view of 10 arcmin for each survey. In cases were sources had weak detection signals, $\sigma_{\rm rms}$ was used to compute the calculated 3σ upper limit for that respective survey (see Table 1). We notice that most of the extended sources (8 out of 11) previously unknown and most were not previously studied in detail (see Appendix A for details on these extended sources).

We will discuss in this paper the nature of the specific source PGC2285791 which is an extended radio galaxy that is poorly

[1] https://third.ucllnl.org/cgi-bin/firstcutout
[2] http://lofar.strw.leidenuniv.nl
[3] http://www.cv.nrao.edu/nvss
[4] http://tgssadr.strw.leidenuniv.nl
[5] http://www.cv.nrao.edu/vlss/VLSSpostage.shtml

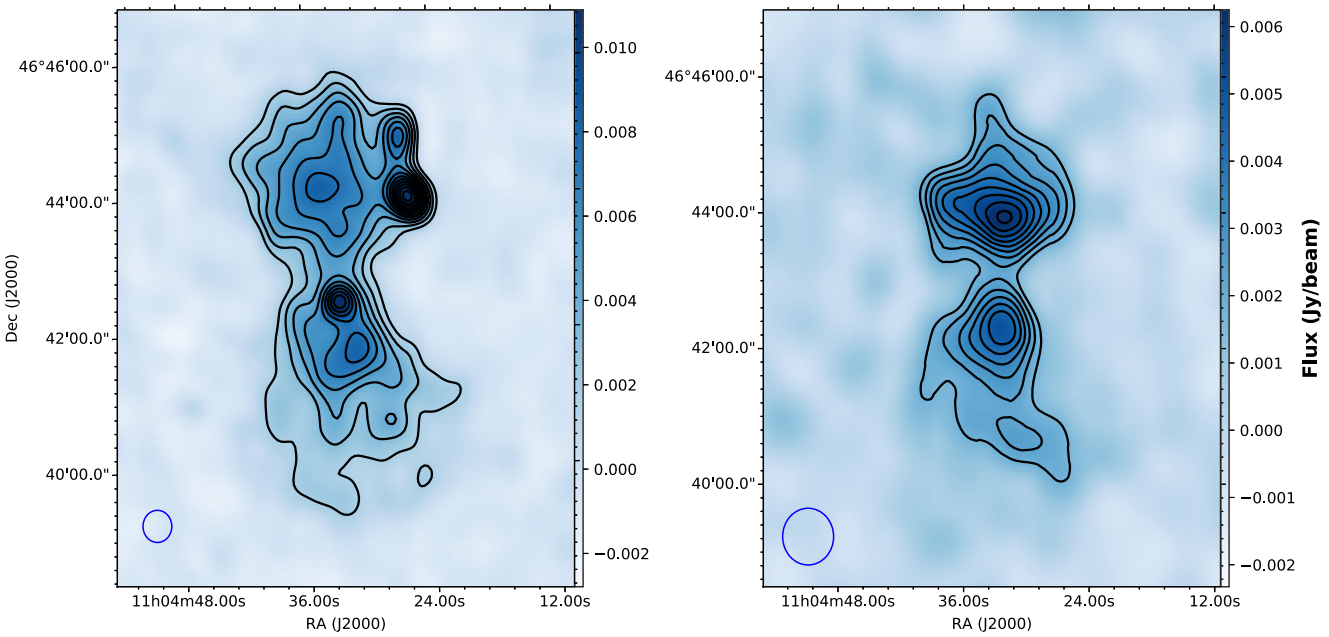

Figure 1. Left: The LoTSS 141 MHz continuum image of PGC2285791 overlaid with black LoTSS contours starting at 3σ ($\sigma = 0.58$ mJy beam^{-1}) with 2σ increments. The beam size of the LoTSS is shown in the lower left corner. Right: The NVSS 1400 MHz continuum image of PGC2285791 overlaid with black NVSS contours starting at 3σ ($\sigma = 0.57$ mJy beam^{-1}) with 1σ increments. The beam size of the NVSS is shown in the lower left corner.

known, while we will present our analysis of the remaining radio sources in a forthcoming paper (Colafrancesco et al. in preparation).

4.1 PGC2285791

The source PGC2285791 (α_{J2000}: $11^h04^m32\overset{s}{.}99$; δ_{J2000}: $+46°42'24\overset{''}{.}83$) is seen as an extended radio source in the LoTSS (see Fig. 1). This source is poorly characterized in the literature and it is listed as a radio galaxy source in Best & Heckman (2012) and Paturel et al. (2003), while it is also identified as a low-redshift source with ultra-steep spectrum in Bornancini et al. (2010). This is the only available information for this source in the literature.

It is justified, therefore, to perform an extensive analysis of this extended radio source based on the LoTSS data.

4.1.1 Morphology

The radio images of PGC2285791 derived from the LoTSS at 141 MHz and the NVSS at 1400 MHz are shown in Fig. 1.

This radio galaxy has two diffuse bright lobes forming a double structure with LoTSS mean surface brightnesses of 3.96 and 2.40 mJy beam^{-1} for the northern and southern lobes, respectively. These lobes are quite irregular, at variance with typical lobes of powerful radio galaxies connected by collimated jets, spanning an overall angular extension of ∼6 arcmin which corresponds to a projected linear size of ∼0.86 Mpc.

The source is also seen to have a similar morphology at 1400 MHz, as shown in Fig. 1. However, we notice that in the LoTSS image the core of the source is brighter and two additional compact sources (or knots) appear in the northern lobe. These two knots have peak LoTSS brightness levels of 8.19 ± 1.00 and 15.26 ± 1.63 mJy pixel^{-1} for the top and bottom knots, respectively, where the pixel size is 11.83 arcsec^2. The region of the northern lobe containing these radio knots has quite steep spectral index (see Fig. 5 and discussion in Section 4.1.5 below).

4.1.2 Integrated spectra

The integrated flux emitted by the core of the radio galaxy is $S_{core(141MHz)} = 8.74 \pm 1.11$ mJy and $S_{core(1400MHz)} = 3.40 \pm 1.07$ mJy. Its radio luminosity is, therefore, $L_{141MHz} \sim 4.35 \times 10^{23}$ W Hz^{-1} and $L_{1400MHz} \sim 1.69 \times 10^{23}$ W Hz^{-1} using the source's luminosity distance of 645 Mpc in the adopted cosmology. The core radio flux density spectrum of the radio galaxy is shown in Fig. 2.

We notice, however, that the spatial resolution of the five radio surveys from which we derived the core flux are quite different, with the VLSSr having the lowest resolution 75 arcsec (the beam size is three times larger than the LoTSS beam), the NVSS having a moderate resolution at 45 arcsec (the beam size is 1.8 times larger than the LoTSS beam) and the FIRST has the highest resolution at 5 arcsec (the beam size is five times smaller than that of the LoTSS beam).

The two knots have an integrated flux of $S_{nk(141MHz)} = 11.26 \pm 1.51$ mJy for the northern knot, and $S_{sk(141MHz)} = 20.53 \pm 1.42$ mJy for the southern knot.

4.1.3 Multi-ν analysis

The core of the radio source PGC2285791 is coincident with an optical and IR source in the ESO-DSS2-red and WISE images (see Fig. 3): this optical source is extended and has the appearance of a galaxy (green square in Fig. 3). The galaxy nature of this source is confirmed by the image and the spectrum of the source as found in the SDSS DR14 (Abolfathi et al. 2018), where it is classified as a star-forming galaxy at redshift $z = 0.14126 \pm 0.00001$ (Adelman-McCarthy et al. 2006). Its optical spectrum is characterized by a number of prominent emission lines, such as, Hα, [N II], [S II], as

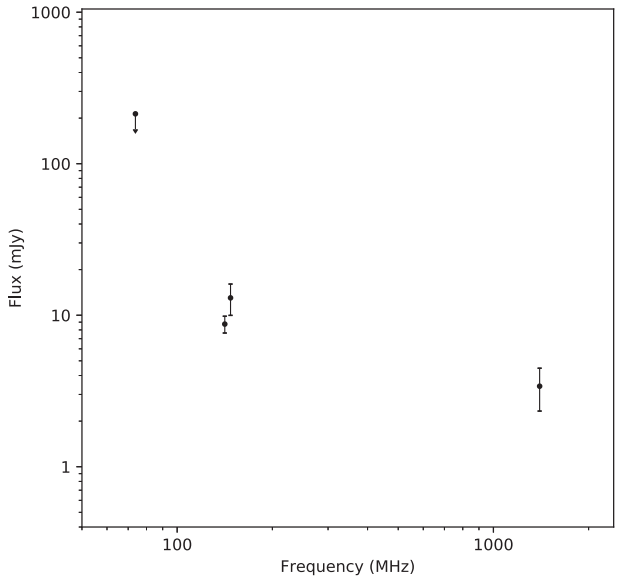

Figure 2. The spectrum of the core of the radio galaxy PGC2285791 is shown for different frequencies, with the frequency–flux pairs (frequency, $S_{\rm core}$) given in Table 2.

well as the forbidden oxygen lines [O II] and [O III]. The source is also associated with a radio galaxy in the QORG catalogue (Flesch & Hardcastle 2004) retrieved from the SSDC Sky Explorer tool[6] denoting its radio galaxy nature.

It is also interesting to notice the presence of two optical sources that lie within the region of the northern lobe (highlighted by yellow and cyan squares in Fig. 3). They have confirmed spectra from SDSS DR14, with the top source being identified as a galaxy at $z = 0.114\,52 \pm 0.000\,03$ (yellow square) and the bottom source identified as PGC2286197 (cyan square), an AGN galaxy at $z = 0.114\,51 \pm 0.000\,03$ with a FIRST radio source in the SSDC Sky Explorer. Even though these two sources are at a comparable redshift to PGC2285791, they appear to be projections that are not interacting with PGC2285791. No optical or IR sources were found at the position of the two radio knots. We will discuss the spectral behaviour of these two knots in Section 4.1.5 below.

The overall multi-ν spectral energy distribution (SED) of the radio galaxy core, obtained from the combination of archival data and of the radio data obtained from this study, is shown in Fig. 4.

The SED of the core is clearly dominated by non-thermal emission at low frequencies while it is dominated by the integrated galaxy emission in the IR and Optical frequency range peaking at $\sim 5 \times 10^{14}$ Hz, and it is quite typical of radio galaxy spectra (Colafrancesco et al. 2016). The lack of high-frequency data in the soft and hard X-ray ranges does not yet allow us to test the inverse Compton (on synchrotron) branch of the core emission. X-ray data would also be crucial in identifying possible inverse Compton scattering X-ray emission from the radio galaxy lobes.

4.1.4 Stellar population properties

We modelled the stellar population of PGC2285791 spectrum obtained from the SDSS DR14 using the full spectral fitting code FIREFLY (Wilkinson et al. 2017) and masking all the emission

[6]https://tools.asdc.asi.it/index.jsp

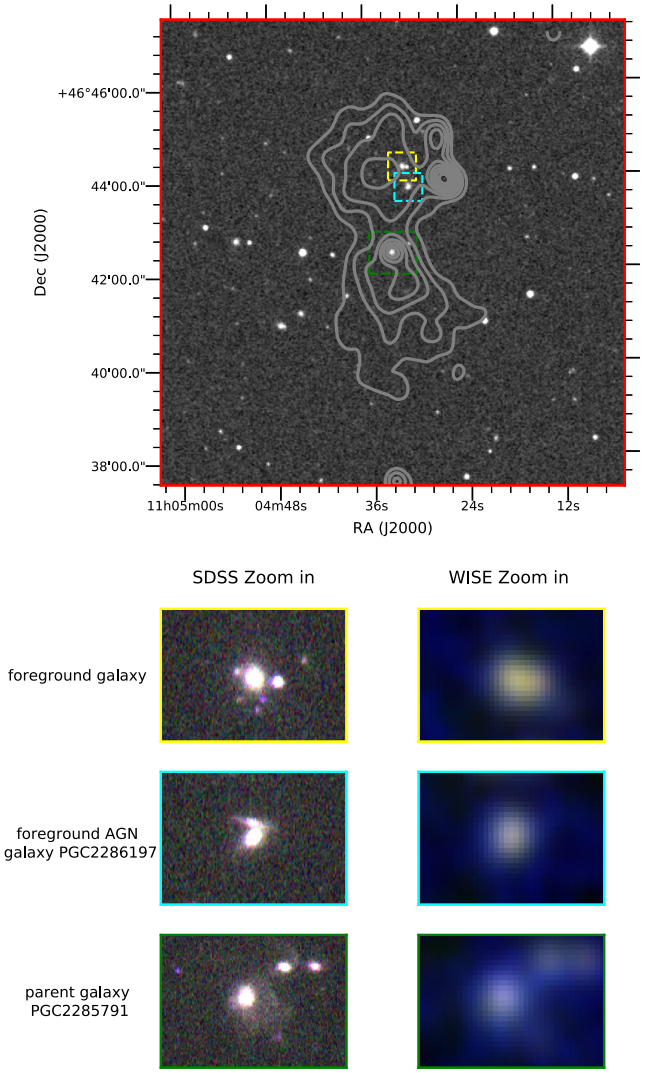

Figure 3. Main: background ESO-DSS2-red image of PGC2285791 overlaid with grey LoTSS contours at [1.74, 3.48, 5.22, 6.96, 8.7, 10.44, 12.18, 13.92, 15.66] mJy beam^{-1}. The green, yellow, and cyan dashed squares are the regions of interests (to be) highlighted by the SDSS *i*, *r*, *g*-band images with corresponding frame colours (below on the left) and the WISE images from the W1, W2, and W3 bands (on the right). Yellow squares: SDSS and WISE zoom-in views of the foreground galaxy. Cyan squares: SDSS and WISE zoom-in views of the foreground AGN galaxy PGC2286197. Green squares: SDSS and WISE zoom-in views of the parent galaxy PGC2285791.

lines. Full details about the modelling process are given in several papers (Wilkinson et al. 2015, 2017; Comparat et al. 2017; Goddard et al. 2017a,b). In short, FIREFLY is a chi-squared minimization fitting code that, for a given input SED, fits combinations of simple stellar populations based on Maraston & Strömbäck (2011) with various input spectral libraries and initial mass functions (IMFs). For our analysis here, we only show stellar population properties (such as age, metallicity, SFR, and black hole mass) derived based on MILES (Sánchez-Blázquez et al. 2006) stellar library with a Charbier (Chabrier 2003) IMF, since it is the best fit in this case. However, we note that a full analysis of the stellar population components is beyond the scope of this work.

None the less, the derived light-weighted average age and metallicity of PGC2285791 are 8.7 Gyr and −0.5 in [Z/H], respectively, with smaller contribution from 10 Myr old and solar

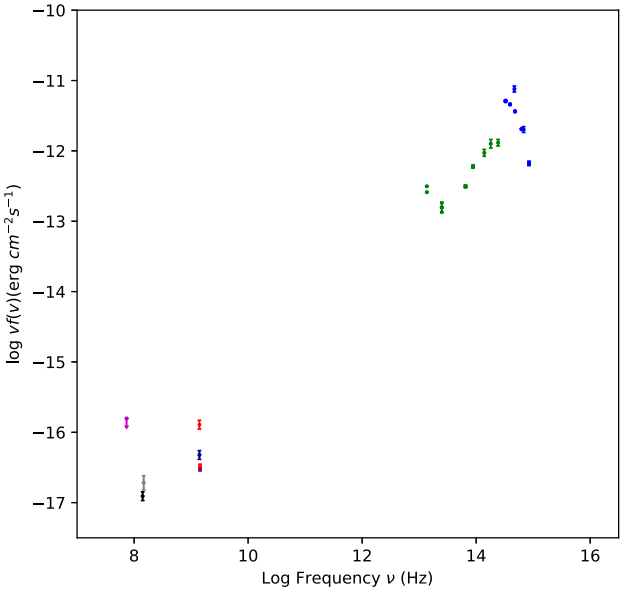

Figure 4. The SED of the core of the radio galaxy PGC2285791 with previously known optical (blue), infrared (green), and radio (red) data points plotted with the addition of the VLSSr upper limit (magenta), LoTSS (black), TGSS ADR1 (grey overlaps with black), NVSS (navy), and FIRST (purple overlaps with red archival data) data points. There are four points in the radio domain that have the same value for the frequency. Starting from the top; the red point is the archival NVSS data point, navy is the NVSS value from this work and the FIRST purple point from this study overlaps with the FIRST archival data point.

metallicity stars. The total and the black hole masses are $\sim 5 \times 10^{10}$ and 2.7×10^8 $M_\odot$, respectively. We have obtained a SFR of ~ 2 $M_\odot$ yr^{-1}.

4.1.5 *Spectral index map*

In order to produce spectral index maps, we aligned the images using MIRIAD (Sault et al. 1995). The higher resolution LoTSS images were smoothed to the lower resolution NVSS images using a Gaussian beam with beam parameters (major='45arcsec', minor = '45arcsec') in MIRIAD.

We then derived the flux densities from each matching pixel coordinate obtained from the two images at different frequencies ($S_{141\mathrm{MHz}}$ and $S_{1400\mathrm{MHz}}$) in order to calculate the spectral index at the corresponding point. The following power-law form of the spectral index formula was used, $S \propto \nu^{\alpha}$, where S is the radio flux density, ν is the frequency, and α is the spectral index. The uncertainties were computed using the relation:

$$\sigma_\alpha = \frac{\sqrt{\left(\frac{\sigma_1}{S_1}\right)^2 + \left(\frac{\sigma_2}{S_2}\right)^2}}{\ln\left(\frac{\nu_1}{\nu_2}\right)}, \qquad (2)$$

where σ_1, σ_2 are the uncertainties of the LoTSS and NVSS flux densities, S_1, S_2 are the integrated flux densities at the LoTSS and NVSS frequency bands (ν_1, ν_2), respectively.

The resulting image array was then imaged in PYTHON using MATPLOTLIB and APLPY (see Fig. 5 for the resulting maps). As we previously cautioned, the lack of access to raw data is a limiting factor and hence our resulting images have not been corrected for direction-dependent effects, which we will leave to the LoTSS survey team.

A two-frequency radio spectral index image was computed from the maps at 141 and 1400 MHz. The distribution of the radio spectral index α is shown in Fig. 5(a) along with the spectral index error map in Fig. 5(b).

The spectral index of the extended radio source PGC2285791 varies from $\alpha = -1.1$ to $\alpha = -0.5$, while the southern radio lobe shows flat spectra with an average value of $\alpha = -0.7$. The emission of the northern lobe has an island of spectral index values that flattens up to $\alpha = -0.6 \pm 0.06$ surrounded by a steeper spectral region including the two radio knots $\alpha = -1.1 \pm 0.06$ towards the north-western boundary. The derived spectral index values are $\alpha_{\mathrm{nk}} = -1.07 \pm 0.06$ and $\alpha_{\mathrm{sk}} = -1.12 \pm 0.06$ for the northern and southern knots, respectively. The spectral index map of the northern lobe indicates the presence of external regions with steep spectra ($\alpha \sim -1.1/-0.9$) which are encasing an inner region with much flatter spectra distribution ($\alpha \sim -0.8/-0.6$).

The southern lobe seems to have a similar structure: the steep spectral index region ($\alpha \sim -1.0/-0.9$) is intermediate between the radio galaxy core and the flatter spectral indices region ($\alpha \sim -0.8/-0.7$) in the outer parts of the lobe.

The spectral index distribution of the radio core is relatively steep ($\alpha \sim -0.8/-0.7$), justifying the decrease of its flux observed from 141 to 1400 MHz.

We note that there are uncertainties in the estimate of the spectral index due to differences in the (u, v) coverage between the two observations; as we can see in the spectral index error map Fig. 5(b) the errors increase slightly towards the edges of the image but are still at a level < 18 per cent.

5 DISCUSSION AND CONCLUSIONS

We have used high-resolution LOFAR images to search for low-surface brightness extended sources at low frequencies. This has enabled us to uncover several either unknown or poorly studied low-surface brightness extended radio sources. Here we presented the specific case of PGC2285791. Our search revealed a very interesting radio morphology and spectral distribution of PGC2285791, enabling us to better characterize the source. We produced spectral index distribution maps by combining the LoTSS image at 141 MHz and NVSS image at 1400 MHz. The spectral index of the extended radio source PGC2285791 varies from $\alpha = -1.1$ to $\alpha = -0.5$. An island of a flat spectral region ($\alpha = -0.6$) and hotspots ($\alpha = -1.0$) are observed. Possible interpretations of the spectral-index variation could be density and magnetic field enhancement due to shock compression by external plasma.

The source exhibits two diffuse bubble-like structures (lobes) on both sides of the core with a projected linear size of 0.84 Mpc. Bubble-like radio structures have also been observed in a few radio galaxies (e.g. Centaurus A (Quillen et al. 2006)) and also in a number of Seyfert and starburst galaxies without obvious jets [e.g. NGC 6764 (Croston et al. 2008), Markarian 6 (Mingo et al. 2011), NGC 3079 (Duric & Seaquist 1988; Shafi et al. 2015)]. Several mechanisms have been suggested for the formation of bubble-like structures in these galaxies. A jet-driven outflow (Quillen et al. 2006) and interaction of starburst wind with ISM are among them (Veilleux, Cecil & Bland-Hawthorn 2005). It is believed that radio galaxies harbour a supermassive black hole (10^8–10^9 $M_\odot$) in their galactic centre which is responsible for launching large-scale radio jets and lobes (Begelman, Blandford & Rees 1984). However, how these jets and lobes grow to their large-

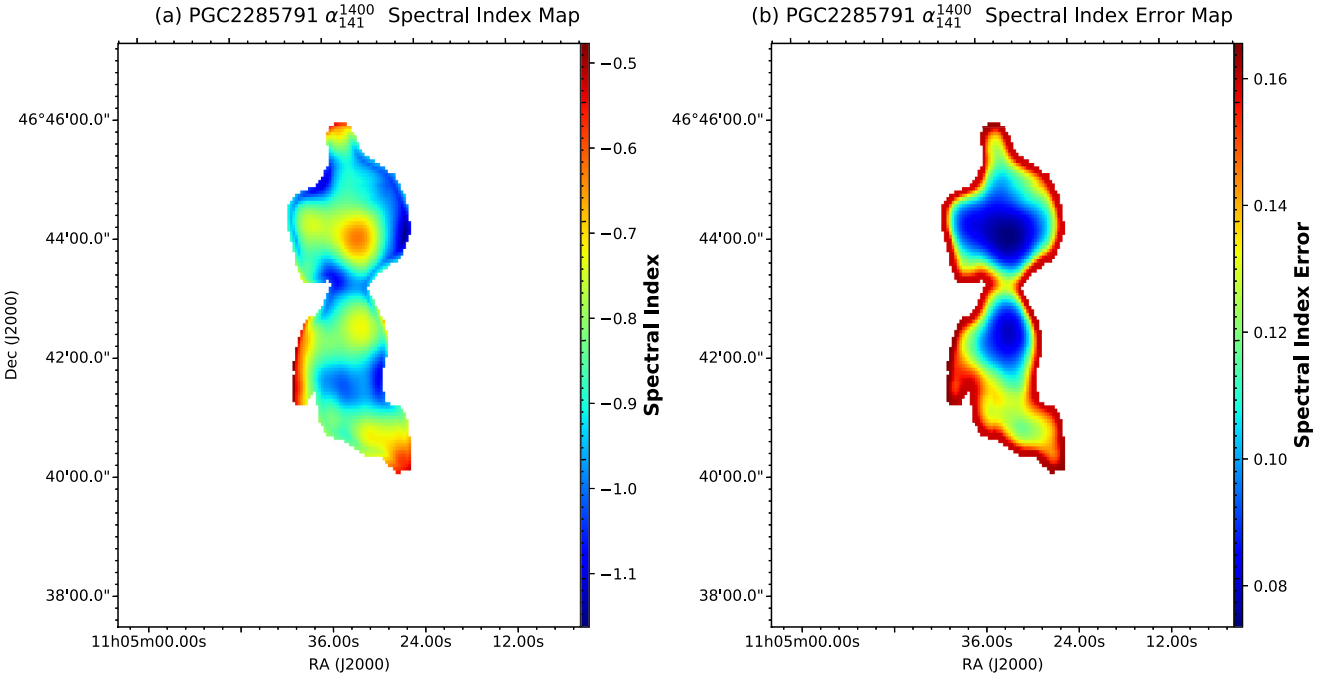

Figure 5. The spectral index (a) and spectral index error (b) maps of PGC2285791 obtained between 141 and 1400 MHz.

scale sizes (>100 kpc in cases such as this), and their impact on the surrounding medium is still not fully understood. The radio jet close to the nucleus of PGC2285791 could possibly give rise to the bubbles of non-thermal radio emission that would interact with the external environment (shock) in the host galaxy. However, wide frequency observations are necessary for detailed spectral index maps and to gain further insight into the physical environment of PGC2285791.

From our analysis of the SDSS spectrum, we see that PGC2285791 is approximated by an 8.7 Gyr old stellar population with lower metallicity. This could be because MILES-based results, though they give the best fit, they tend to have their minimum χ^2 values at higher age, but a lower metallicity (Wilkinson et al. 2017). However, if correctly represented, then the low metallicity could be reflective of gas outflow and the interplay between the galaxy's ISM and the IGM. On the other hand, star formation may have been triggered by galaxy mergers or interaction, though we did not see any sign of interaction or disturbance.

In addition, in a simplified emission line diagnostics based on different line ratio diagrams in Kewley et al. (2006) classification (see Kewley et al. (2006) and references for details), PGC2285791 seems to fall under composite sources. While the lack of noticeable line-broadening in the optical spectrum suggests a type 2 AGN, the prominent emission line features could be from nuclear starbursts that are a few Myr old. However, unless we have spatially resolved observation, it is often difficult to disentangle the contributions of the two to the emission line spectrum. We note that a better understanding of the star-forming and AGN nature of the source and how it affects the physical properties of the source requires a more in depth analysis of the ionization properties as well as the gas kinematics. The next generation radio telescopes such as ASKAP and MeerKAT would be very useful to investigate the physical conditions and kinematics of the gas in low surface brightness radio galaxies.

Finally, our study shows the value of the high resolution and high sensitivity of LOFAR maps for studies of low surface brightness sources, and in particular radio galaxies with extended lobes.

ACKNOWLEDGEMENTS

We thank the Referee for several useful comments and suggestions. This work is based on the research supported by the South African Research Chairs Initiative (SARChI) of the Department of Science and Technology (DST) and National Research Foundation (NRF) of South Africa (Grant No 77948). SAT acknowledges support from the DST/NRF SKA post-graduate bursary initiative. This research has made use of the NASA/IPAC Extragalactic Database (NED), which is operated by the Jet Propulsion Laboratory, California Institute of Technology, under contract with the National Aeronautics and Space Administration.

REFERENCES

Abolfathi B. et al., 2018, ApJS, 235, 42
Adelman-McCarthy J. K. et al., 2006, ApJS, 162, 38
Barber T., Meiksin A., Murphy T., 2007, MNRAS, 377, 787
Becker R. H., White R. L., Edwards A. L., 1991, ApJS, 75, 1
Becker R. H., White R. L., Helfand D. J., 1995, ApJ, 450, 559
Begelman M. C., Blandford R. D., Rees M. J., 1984, Rev. Mod. Phys., 56, 255
Best P. N., Heckman T. M., 2012, MNRAS, 421, 1569
Best P. N., Kauffmann G., Heckman T. M., Ivezić Ž., 2005, MNRAS, 362, 9
Blanton M. R. et al., 2017, AJ, 154, 28

Bornancini C. G., O'Mill A. L., Gurovich S., Lambas D. G., 2010, MNRAS, 406, 197
Brienza M. et al., 2016, A&A, 585, 29
Cantwell T. M., Scaife A. M. M., Oozeer N., Wen Z. L., Han J. L., 2016, MNRAS, 458, 1803
Chabrier G., 2003, PASP, 115, 763
Cohen A. S., Lane W. M., Cotton W. D., Kassim N. E., Lazio T. J. W., Perley R. A., Condon J. J., Erickson W. C., 2007, AJ, 134, 1245
Colafrancesco S., Mhlahlo N., Jarrett T., Oozeer N., Marchegiani P., 2016, MNRAS, 456, 512
Comparat J. et al., 2017, preprint (arXiv:1711.06575)
Condon J. J., Cotton W. D., Greisen E. W., Yin Q. F., Perley R. A., Taylor G. B., Broderick J. J., 1998, AJ, 115, 1693
Croston J. H., Hardcastle M. J., Kharb P., Kraft R. P., Hota A., 2008, ApJ, 688, 190
Duric N., Seaquist E. R., 1988, ApJ, 326, 574
Fanti C., Fanti R., 1994 , in Bicknell G. V., Dopita M. A., eds, ASP Conf. Ser. Vol. 54, The First Stromlo Symposium: The Physics of Active Galaxies. Astron. Soc. Pac., San Francisco, 341
Farnes J. S., Gaensler B. M., Carretti E., 2014, ApJS, 212, 15
Ficarra A., Grueff G., Tomassetti G., 1985, A&AS, 59, 255
Flesch E., Hardcastle M. J., 2004, A&A, 427, 387
Goddard D. et al., 2017a, MNRAS, 465, 688
Goddard D. et al., 2017b, MNRAS, 466, 4731
Green D. A., Riley J. M., 1995, MNRAS, 274, 324
Gregory P. C., Condon J. J., 1991, ApJS, 75, 1011
Gregory P. C., Scott W. K., Douglas K., Condon J. J., 1996, ApJS, 103, 427
Hales S. E. G., Baldwin J. E., Warner P. J., 1988, MNRAS, 234, 919
Holt J., Tadhunter C., Morganti R., Bellamy M., González Delgado R. M., Tzioumis A., Inskip K. J., 2006, MNRAS, 370, 1633
Holt J., Tadhunter C. N., Morganti R., 2008, MNRAS, 387, 639
Intema H. T., Jagannathan P., Mooley K. P., Frail D. A., 2017, AAP, 598, A78
Kewley L. J., Groves B., Kauffmann G., Heckman T., 2006, MNRAS, 372, 961
Lane W. M., Cotton W. D., van Velzen S., Clarke T. E., Kassim N. E., Helmboldt J. F., Lazio T. J. W., Cohen A. S., 2014, MNRAS, 440, 327
Lin Y.-T., Shen Y., Strauss M. A., Richards G. T., Lunnan R., 2010, ApJ, 723, 1119
Maraston C., Strömbäck G., 2011, MNRAS, 418, 2785
Maslowski J., Pauliny-Toth I. I. K., Witzel A., Kuehr H., 1984, AAP, 139, 85
Massaro F., Giroletti M., D'Abrusco R., Masetti N., Paggi A., Cowperthwaite P. S., Tosti G., Funk S., 2014, ApJS, 213, 3
McMahon R. G., White R. L., 2002, ApJS, 143, 1
Mingo B., Hardcastle M. J., Croston J. H., Evans D. A., Hota A., Kharb P., Kraft R. P., 2011, ApJ, 731, 21
Mohan N., Rafferty D., 2015, Astrophysics Source Code Library, record ascl:1502.007
Mulcahy D. D. et al., 2014, AAP, 568, A74
O'Dea C. P. et al., 2002, AJ, 123, 2333
Paturel G. et al., 2003, AAP, 412, 45
Pooley G. G., Kenderdine S., 1968, MNRAS, 139, 529
Quillen A. C., Bland-Hawthorn J., Brookes M. H., Werner M. W., Smith J. D., Stern D., Keene J., Lawrence C. R., 2006, ApJ, 641, L29
Sault R. J., Teuben P. J., Wright M. C. H., 1995 , in Shaw R. A., Payne H. E., Hayes J. J. E., eds, ASP Conf. Ser. Vol. 77, Astronomical Data Analysis Software and Systems IV. Astron. Soc. Pac., San Francisco, p. 433
Shafi N., Oosterloo T. A., Morganti R., Colafrancesco S., Booth R., 2015, MNRAS, 454, 1404
Shimwell T. W. et al., 2017, A&A, 598, A104
Subrahmanyan R., Saripalli L., Hunstead R. W., 1996, MNRAS, 279, 257
Szabo T., Pierpaoli E., Dong F., Pipino A., Gunn J., 2011, ApJ, 736, 21
Sánchez-Blázquez P. et al., 2006, MNRAS, 371, 703
van Haarlem M. P. et al., 2013, A&A, 556, 2
Veilleux S., Cecil G., Bland-Hawthorn J., 2005, ARA&A, 43, 769
Vollmer B. et al., 2010, AAP, 511, A53
West A. A., Hawley S. L., Bochanski J. J., Covey K. R., Reid I. N., Dhital S., Hilton E. J., Masuda M., 2008, AJ, 135, 785
West A. A. et al., 2011, AJ, 141, 97
Wilkinson D. M., Maraston C., Goddard D., Thomas D., Parikh T., 2017, MNRAS, 472, 4297
Wilkinson D. M. et al., 2015, MNRAS, 449, 328
Wright E. L. et al., 2010, AJ, 140, 1868

APPENDIX A: KNOWN INFORMATION ABOUT THE EXTENDED SOURCES FROM THE LITERATURE

There are in total three sources which have an identification in the literature, namely: PGC2285791, PGC2396883, and B31059 + 460. These sources, as well as the eight remaining sources, have only little information available in the literature, which we detail below.

(i) Source 01 has been classified as a flat-spectrum source (Massaro et al. 2014), while it also appears in the SPECFIND V2.0 catalogue tool (Vollmer et al. 2010) and the 5C2 survey (Pooley & Kenderdine 1968).

(ii) We found that the sources 02 and 11 have no prior information available in the literature.

(iii) Source 03 only appears in Vollmer et al. (2010; The SPECFIND V2.0 catalogue of radio cross-identifications and spectra. SPECFIND meets the Virtual Observatory).

(iv) The source B31059 + 460 appears in various catalogues described in Ficarra, Grueff & Tomassetti (1985), Hales, Baldwin & Warner (1988), Becker, White & Edwards (1991), Gregory & Condon (1991), Green & Riley (1995), Gregory et al. (1996), McMahon & White (2002), Cohen et al. (2007), Vollmer et al. (2010), Farnes, Gaensler & Carretti (2014).

(v) Both of the studies (West et al. 2008, 2011) associated with the source 05 are from the SDSS spectroscopic catalogue, which classify this source as an M-Dwarf star.

(vi) The source 06 is associated with the galaxy PGC2285791 (Paturel et al. 2003; Best & Heckman 2012), and due to its interesting extended radio emission it is the main subject of our study, and discussed in detail in Section 4.1.

(vii) Sources 07 and 10 have been identified as optical galaxy clusters, using an adaptive matched filter technique described in Szabo et al. (2011).

(viii) Source 08 is a $z = 0.31$ radio galaxy that seems to be in the same field of view as a well-studied QSO source at $z = 2.22$.

(ix) The source 09 is associated with the galaxy PGC2396883 which has been part of a few statistical studies (Barber, Meiksin & Murphy 2007; Lin et al. 2010) and also appears in the following catalogues (Maslowski et al. 1984; Paturel et al. 2003; Best et al. 2005; Best & Heckman 2012; Farnes et al. 2014).

Table A1. Data on the studied extended sources detected by *LoTSS*. Column (1): Radio source names; Column (2) and (3): Right Ascension (J2000) and Declination (J2000); Column (4)–(8): integrated flux densities of the extended radio sources; Column (9): two-frequency radio spectral index between 141 (LoTSS) and 1400 MHz (NVSS).

			Integrated flux density (mJy)					Spectral index[a]
Source name	RA (J2000)	Dec. (J2000)	VLLSr	LoTSS	TGSS ADR1	NVSS	FIRST	α_{141}^{1400}
			73.8 MHz	141 MHz	150 MHz	1400 MHz	1400 MHz	
(1)	(2)	(3)	(4)	(5)	(6)	(7)	(8)	(9)
Source 01	10 51 33.43	+ 50 12 53.84	305.41 ± 117.0	247.71 ± 24.77	91.84 ± 9.19	46.35 ± 4.63	24.24 ± 2.43	−0.73 ± 0.06
Source 02	11 00 48.28	+ 45 51 41.83	300.00[b] ± 45.00	154.21 ± 15.42	15.52 ± 1.56	10.91 ± 1.09	1.49 ± 0.15	−1.16 ± 0.06
Source 03	11 01 29.19	+ 46 00 27.50	701.96 ± 70.20	385.87 ± 38.59	310.34 ± 3.57	5.13 ± 1.64	8.39 ± 0.84	−1.88 ± 0.15
B31059 + 460	11 02 50.47	+ 45 44 38.40	394.47 ± 39.45	454.10 ± 45.41	380.72 ± 38.07	76.04 ± 7.60	81.16 ± 8.12	−0.78 ± 0.06
Source 05	11 03 39.37	+ 45 50 08.58	300.00[b] ± 45.00	233.14 ± 23.31	78.96 ± 7.90	16.87 ± 1.69	9.45 ± 0.95	−1.15 ± 0.06
PGC2285791	11 04 32.99	+ 46 42 24.83	300.00[b] ± 45.00	301.20 ± 30.12	28.40 ± 10.56	45.93 ± 4.59	2.10 ± 0.25	−0.82 ± 0.06
Source 07	11 07 57.85	+ 51 20 23.88	300.00[b] ± 45.00	315.70 ± 20.50	172.35 ± 17.23	4.31 ± 0.43	3.03 ± 0.30	−1.87 ± 0.05
Source 08	11 09 41.77	+ 44 58 27.48	300.00[b] ± 45.00	204.99 ± 20.50	15.00[b] ± 1.50	32.95 ± 3.29	30.22 ± 3.02	−0.80 ± 0.06
PGC2396883	11 11 57.61	+ 51 36 21.30	300.00[b] ± 45.00	175.54 ± 17.55	48.63 ± 4.87	35.70 ± 3.57	12.87 ± 1.28	−0.69 ± 0.06
Source 10	11 27 13.17	+ 51 13 25.91	300.00[b] ± 45.00	140.00 ± 14.00	35.61 ± 3.04	16.43 ± 1.20	3.82 ± 0.38	−0.93 ± 0.05
Source 11	11 32 50.56	+ 50 57 04.25	300.00[b] ± 45.00	99.28 ± 9.93	39.01 ± 3.35	14.65 ± 1.46	9.08 ± 0.91	−0.83 ± 0.06

Notes: [a]The convention, $S \propto \nu^{\alpha}$, was used to calculate the spectral index, where S is the radio flux density, ν is the frequency, and α is the spectral index.

[b]The calculated 3σ upper limit, from the respective survey, was used for instances where the radio survey provided a weak detection.

This paper has been typeset from a TEX/LATEX file prepared by the author.